Kelvin Waves during GOAmazon and Their Relationship to Deep Convection

YOLANDE L. SERRA

University of Washington Cooperative Institute for Climate, Ocean, and Ecosystem Studies, Seattle, Washington

ANGELA ROWE

University of Wisconsin–Madison, Madison, Wisconsin

DAVID K. ADAMS

Universidad Nacional Autónoma de México, Mexico City, Mexico

GEORGE N. KILADIS

National Oceanic and Atmospheric Administration, Silver Spring, Maryland,

(Manuscript received 9 January 2020, in final form 5 August 2020)

ABSTRACT: The 2014–15 Observations and Modeling of the Green Ocean Amazon (GOAmazon) field campaign over the central Amazon near Manaus, Brazil, occurred in coordination with the larger Cloud Processes of the Main Precipitation Systems in Brazil: A Contribution to Cloud-Resolving Modeling and to the Global Precipitation Measurement (CHUVA) project across Brazil. These programs provide observations of convection over the central Amazon on diurnal to annual time scales. In this study, we address the question of how Kelvin waves, observed in satellite observations of deep cloud cover over the GOAmazon region during the 2014–15 time period, modulate the growth, type, and organization of convection over the central Amazon. The answer to this question has implications for improved predictability of organized systems over the region and representation of convection and its growth on local to synoptic scales in global models. Our results demonstrate that Kelvin waves are strong modulators of synoptic-scale low- to midlevel free-tropospheric moisture, integrated moisture convergence, and surface heat fluxes. These regional modifications of the environment impact the local diurnal cycle of convection, favoring the development of mesoscale convective systems. As a result, localized rainfall is also strongly modulated, with the majority of rainfall in the GOAmazon region occurring during the passage of these systems.

KEYWORDS: Amazon region; Convective-scale processes; Mesoscale processes; Water vapor; Intraseasonal variability; Tropical variability

1. Introduction

Deficiencies in knowledge and difficulties in modeling convective processes in tropical regions, particularly the uncertain role of aerosols in convective growth and intensity, motivated the 2014–15 Observations and Modeling of the Green Ocean Amazon (GOAmazon; Martin et al. 2017) field campaign. This major campaign occurred in coordination with the larger Cloud Processes of the Main Precipitation Systems in Brazil: A Contribution to Cloud-Resolving Modeling and to the Global Precipitation Measurement (CHUVA) project across Brazil (Machado et al. 2014). The heavily instrumented 2014–15 period of these campaigns captured temporal variability of convective systems in the central Amazon near Manaus, Brazil (3°S, 60°W), across seasonal, synoptic, and diurnal time scales, while also measuring spatial variations in cloud–aerosol–precipitation interactions (e.g., Machado et al. 2014; Martin et al. 2016, 2017; Fan et al. 2018).

This study focuses on the wet season over the Amazon, which arrives as the monsoon system of the Americas develops across South America starting in late November or early December over central Brazil, moving north and south as the season progresses, with the monsoon rains continuing into May for the equatorial regions (Vera et al. 2006; Grimm 2011). At the peak of the monsoon, the surface low pressure (Chaco low) deepens over northern Argentina on the east side of the Andes and drives important moisture transport from the tropical Atlantic, across the central Amazon and into subtropical South America as part of the South American monsoon circulation (Vera et al. 2006; Grimm 2011; Grimm and Silva Dias 2011; Gimeno et al. 2012; Marengo et al. 2012). A characteristic southeast-oriented rainband extending from the southern Amazon, across central South America, and into the southeast Atlantic known as the South Atlantic convergence zone (SACZ) forms during the austral summer in association with the monsoon circulation (Vera et al. 2006). When the low-level northwesterly flow intensifies within a narrow region along the east side of the Andes it forms what is known as the South American low-level jet (SALLJ) (Vera et al. 2006). This jet is responsible for a significant portion of the mass and water transport from the Amazon to subtropical latitudes throughout the year with peak transports observed during the monsoon (Vera et al. 2006; Marengo et al. 2012; Martinez and Dominguez 2014). Variability in this jet occurs on diurnal to

Corresponding author: Yolande L. Serra, yserra@uw.edu

DOI: 10.1175/JAS-D-20-0008.1

interannual time scales affecting moisture transport and convective development within southeast South America, including the SACZ (Marengo et al. 2012; Martinez and Dominguez 2014). The GOAmazon/CHUVA study region is located north and east of the main SACZ in what is referred to throughout this text as the central Amazon.

On synoptic scales, squall lines form over the northern coast of Brazil and propagate southwestward across northern South America (Cohen et al. 1995; Betts et al. 2009; Alcântara et al. 2011). The frequency of these squall lines contributes to the overall frequency of rain events in the central Amazon primarily during March and October (Machado et al. 2004). In addition, Kelvin waves are observed over the central Amazon with the highest frequency of occurrence from November to April during the wet season (Liebmann et al. 2009). As a predominant feature of the tropical circulation (e.g., Takayabu and Murakami 1991; Takayabu 1994; Dunkerton and Crum 1995; Wheeler and Kiladis 1999; Wheeler et al. 2000; Straub and Kiladis 2002; Roundy 2008), eastward-propagating Kelvin waves modulate deep convection, with their convective envelopes composed of a variety of mesoscale elements propagating primarily westward, some of which include westward inertio-gravity (WIG) waves (Kiladis et al. 2009; Tulich and Kiladis 2012). Over South America, WIG waves have been linked to the squall lines that propagate across the Amazon from the Atlantic coast (Tulich and Kiladis 2012).

Despite these initial studies indicating a modulation of convection over the central Amazon on synoptic time scales, the link between these scales and the shallow-to-deep transition over this region has yet to be investigated. At the same time, recent results suggest organized mesoscale convective systems (MCSs) contribute to the majority of rainfall over the central Amazon throughout the year (Rehbein et al. 2017, 2019) and the results of the present study support this finding. Thus, it is of interest to improve understanding of the processes associated with synoptic systems that favor the organization of convection over the region.

The current study approaches this knowledge gap by examining how convection develops with respect to Kelvin waves during the GOAmazon period, as these waves are found to have a significant impact on the frequency of MCSs over the GOAmazon region. Through ground-based measurements of rainfall, clouds, and MCSs collected during GOAmazon/CHUVA, along with a dense network of precipitable water vapor (PWV) data from global positioning system (GPS) receivers (Adams et al. 2015, 2017), the impact of Kelvin waves on the regional- and local-scale environment and on convective development is explored. Specifically, we aim to address the following questions: 1) What is the Kelvin wave activity during GOAmazon? 2) How do Kelvin waves impact the local and regional-scale thermodynamic and dynamic environment? 3) What is the impact of Kelvin waves on deep convective activity over the central Amazon?

2. Data and methods

The seasonal cycle is complex across the Amazon, varying significantly from north to south and east to west (Betts et al. 2009; Grimm 2011; Marengo et al. 2012). For the central Amazon region near Manaus, we define the wet season as December through April, the transition season from wet to dry as May and June, the dry season as July through September, and the transition season from dry to wet as October and November, based on previous studies (Grimm 2011; Marengo et al. 2012; Zhuang et al. 2017) as well as on the rainfall patterns observed during the 2014–15 season over this region.

a. GOAmazon dataset

The Department of Energy (DOE) Atmospheric Radiation Measurement (ARM) program mobile facility (AMF) was deployed at Manacapuru, Brazil (T3: 3.21°S, 60.60°W; Fig. 1), during GOAmazon2014–15. Included in this mobile facility deployment were surface meteorological observations along with ground-based remote sensing measurements of clouds and precipitation collected nominally from 15 January 2014 to 1 December 2015. Surface precipitation at T3 is provided from an acoustic rain gauge with a piezoelectrical sensor (AOSMET), an optical rain gauge (MAOMET), a tipping-bucket rain gauge (TBRG), and a disdrometer (PARS2). As part of the AMF at T3, radiosondes were launched four to six times daily providing vertical profiles of temperature, humidity, and winds (SONDE). We also make use of the AMF microwave radiometer (MWR) observations at T3 for integrated column water vapor. In addition to these standard AMF products, cloud fraction is available through the Merged Cloud Mask and Cloud Type data product (McFarlane et al. 2013; Burleyson et al. 2015; Giangrande et al. 2017; Feng and Giangrande 2018) that combines the calibrated radar wind profiler (RWP) reflectivity data with the W-Band Cloud Radar Active Remote Sensing of Cloud product (WACRARSCL; Clothiaux et al. 2000; Kollias et al. 2005); the latter uses cloud radar data with collocated micropulse lidar and ceilometer data to produce cloud boundaries in time and height. The WACRARSCL and RWP products were downsampled to 20 s, with the former retaining its 30-m vertical resolution and the RWP vertically interpolated to that same ARSCL 30-m grid. The estimated cloud types from this merged product are available every 30 min from 19 February 2014 through 30 November 2015 and includes seven cloud types on a 30-m vertical grid: shallow cumulus, congestus, deep convective clouds, altocumulus, altostratus, cirrostratus, and cirrus. The data products at T3 used for this study are identified by the names shown in parentheses next to their description throughout this section.

b. SIPAM radar data

This study makes use of the operational S-band Doppler radar [the Amazon Protection System (SIPAM)] located at Ponta Pelada, Brazil (3.15°S, 59.99°W; Fig. 1). With an operating range of 150 km, this radar overlaps the T3 site and provides broader spatial context for systems impacting the vertically pointing ARM instrumentation at that location. SIPAM data are available from 3 January 2014 through 31 December 2015, with data gaps during the 3–11 November 2014 period due to a radar malfunction. This study uses version 2.0 of the gridded SIPAM data released by Texas A&M University (Schumacher and Funk 2018) and available on the ARM data archive (SIPAM-S-BAND-CAPPI), with 2-km horizontal and 0.5-km vertical spacing. The Tropical Rainfall Measuring Mission (TRMM)-derived calibration offsets were

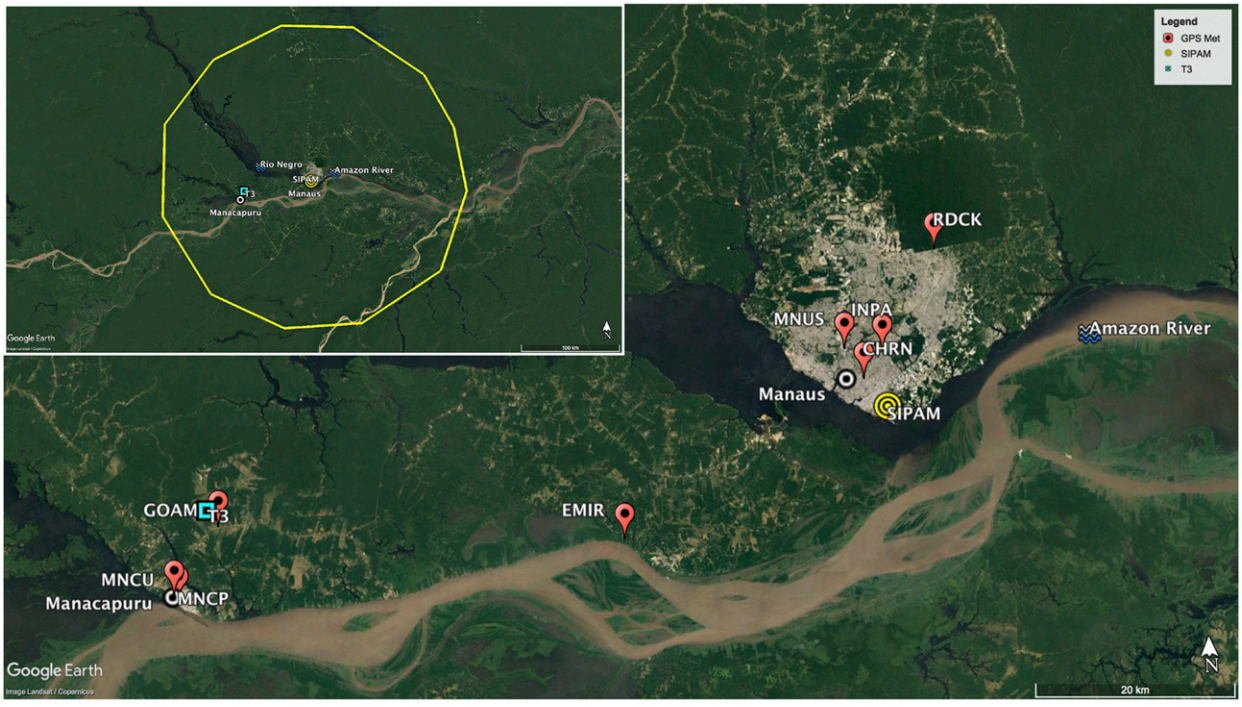

FIG. 1. Map of the GNSS network during GOAmazon. Also indicated is the main DOE AMF site (T3) and the location of the operational radar (SIPAM). Inset shows an overview of the GOAmazon site within the 150-km range ring of the SIPAM radar (yellow circle).

applied to radial radar data before interpolation to a fixed Cartesian grid. A fuzzy logic classifier was created to identify and remove nonmeteorological echo. The number of elevation angles varies with volume, which has implications for this gridded dataset. To mitigate potential effects of gaps in interpolated fields, this study focuses only on a 100-km range from SIPAM.

For this analysis, a feature-based identification algorithm (Rowe and Houze 2014) is applied to the 2.5-km-height gridded SIPAM reflectivity data. In this method, contiguous echo meeting a 20-dBZ threshold is assigned a unique feature identifier. An ellipse-fitting method provides horizontal dimensions of these features and a 100-km major axis threshold is applied to distinguish MCS from sub-MCS features. The thresholds applied to this study ensure that any remaining clutter is neglected (20-dBZ threshold) and that larger organized systems (100-km threshold) can be related to the Kelvin wave activity using the Kelvin wave index described in section 2d. Radar-derived rain rates are also provided (SIPAM-S-BAND-RAIN), where a single Z–R relationship of $Z = 174.8R^{1.56}$ is applied to the corrected gridded reflectivity field at the 2.5-km height level. This Z–R relation was derived from the Parsivel^2 disdrometer data at the ARM T3 site during the 2014 wet season (Schumacher and Funk 2018).

c. Large-scale environmental data

The large-scale atmospheric conditions analyzed in this study are provided by the European Centre for Medium-Range Weather Forecasts (ECMWF) interim reanalysis (ERA-Interim, hereafter ERAI) available at 37 pressure levels on a native 0.7° × 0.7° global grid and 6-hourly time resolution since 1979 (Dee et al. 2011). In addition, we make use of the constrained variational analysis product for GOAmazon (VARANAL; Tang et al. 2016) to capture the regional-scale variations in vertical dynamic and thermodynamic structure associated with the waves and the diurnal cycle in convection. This product uses the ECMWF 0.5° × 0.5° analysis fields together with top of the atmosphere and surface observations from GOAmazon to constrain vertically integrated mass, water, and dry static energy. Adjustments of the upper-level fields in the analyses are made until these budgets close within a specified tolerance (Tang et al. 2016, and references therein). As the VARANAL is also constrained by the SIPAM radar domain rainfall (section 2b), the vertical integral of $Q_1 - Q_{\mathrm{rad}}$, where Q_1 and Q_{rad} are the net diabatic and radiative heating profiles, respectively, is consistent with the observed rainfall (Tang et al. 2016). The latest version of the VARANAL uses the 2-m rainfall from the SIPAM radar but is unable to make use of the GOAmazon radiosonde observations due to a lack of spatial representativeness across the domain used for the integration. Thus, the radiosondes at T3 offer an independent measure of the variability in the vertical structure from that of the VARANAL product.

d. Kelvin wave identification

Kelvin waves are isolated through space–time filtering of outgoing longwave radiation (OLR) following the method of Wheeler and Kiladis (1999). The space–time filter used for this study selects for 2.5–17-day eastward-propagating disturbances with global (zonal) wavenumbers between 1 and 14 between

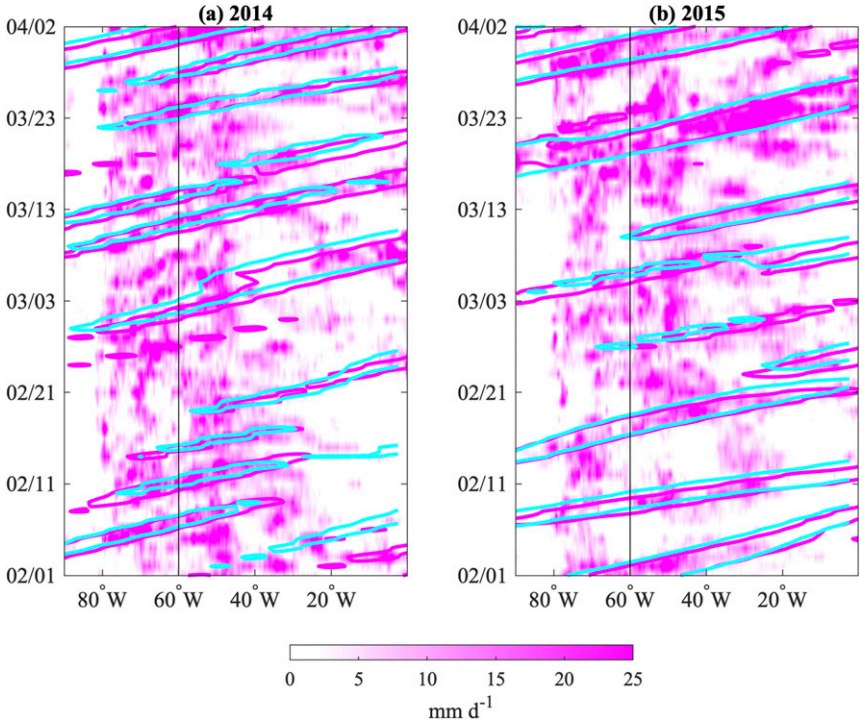

FIG. 2. Hovmöller plots of TRMM 0.25° × 0.25° daily rainfall over South America averaged from 5°S to 2°N for February–March of (a) 2014 and (b) 2015 with the 2 mm day^{-1} Kelvin-filtered TRMM rainfall contour (magenta). The −7 W m^{-2} contour (cyan) of Kelvin-filtered OLR averaged from 5°S to 2.5°N is also shown. The vertical black line in each panel indicates the location of T3.

equivalent depth curves of 8 and 90 m, using NOAA Climate Diagnostics Center (CDC) twice daily 2.5° × 2.5° OLR fields from 1980 to 2015. This same filter was also used on the TRMM 3B42 daily 0.25° × 0.25° rainfall product. Figure 2 shows Hovmöller diagrams of daily TRMM rainfall for February and March of 2014 and 2015 averaged from 5°S to 2°N over South America along with the 2 mm day^{-1} contour of Kelvin-filtered rainfall. The −7 W m^{-2} contour of Kelvin-filtered OLR averaged from 5°S to 2.5°N is also shown. (The northern latitude is slightly different from that used for TRMM, as the first grid point north of the equator is 2.5° for OLR.) The Kelvin-filtered rainfall and OLR contours represent one standard deviation in these indices at the longitude of T3 over the latitude band shown. The Kelvin waves propagating from the west across the region exhibit more activity during 2014 than during 2015; however, the 2015 disturbances appear more coherent in both rainfall and OLR signals (e.g., the event crossing T3 on 20 March 2015). The precipitation signal of most of the Kelvin waves appears to originate over the western Amazon, with few signals initiating west of the Andes (around 80°W at these latitudes), although this does not preclude drier dynamical signals that might originate over the Pacific (Liebmann et al. 2009). While there are often stationary or westward-propagating rainy regions within this latitude band, the Kelvin wave signals are more often associated with the larger convective elements and are thus the focus of this study.

To obtain the characteristic structure of the Kelvin wave activity over the Amazon, we regress ERAI pressure level and vertically integrated quantities, as well as OLR, onto Kelvin-filtered OLR at T3 for the 2014–15 time period, matching the reanalysis times to those of the filtered OLR. Lagged regressions are constructed by shifting the dependent variable in time with respect to Kelvin-filtered OLR. The 2014–15 daily means at each grid point are removed prior to calculating the regressions. Removal of the daily means together with regression onto filtered OLR effectively isolates Kelvin wave related anomalies from seasonal and shorter period wave (such as WIG wave) anomalies in the reanalysis and OLR fields.

We define the twice daily time series of Kelvin-filtered OLR at T3 as our Kelvin wave index (olrkel). We then define days of suppressed (olrkel $> +1.5\sigma$), neutral ($-1.5\sigma \leq$ olrkel $\leq +1.5\sigma$), and active (olrkel $< -1.5\sigma$) convective anomalies associated with the Kelvin waves using this index, where σ is the standard deviation of the index over the 1980–2015 time period. The 1.5σ threshold is the same as that used by Liebmann et al. (2009), who note that weaker wave activity and their associated convective anomalies may be missed by this threshold. Because WIG waves are also active over this region (Tulich and Kiladis 2012), a similar index is constructed for those disturbances, also using a 1.5σ threshold to isolate active, suppressed, and neutral convective days with respect to WIG waves at T3. The space–time filter used for WIG waves selects for 1.4–3.3-day westward-

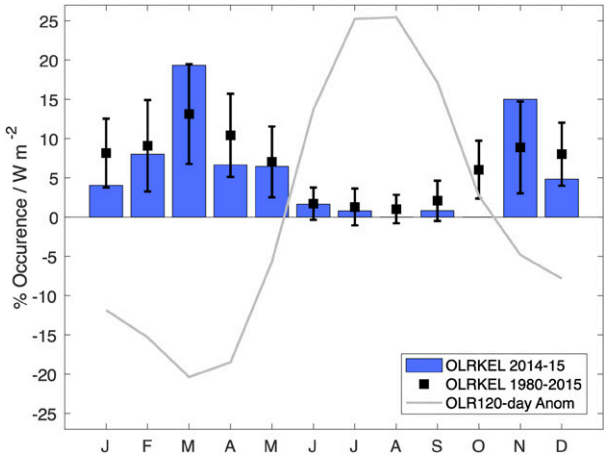

FIG. 3. Kelvin wave activity at T3 as measured by percent occurrence of filtered anomalies less than -1.5σ for the 1980–2015 (squares) and 2014–15 (bars) time periods. Error bars indicate the standard deviation in the percent Kelvin activity for that month over all years for the climatology. The 1980–2015 anomalies in monthly mean 120-day low-pass-filtered OLR (gray line) are also shown as an indicator of the wet and dry seasons.

propagating disturbances with global (zonal) wavenumbers between -15 and -1 between equivalent depth curves of 12 and 50 m. The Kelvin active, suppressed, and neutral convective days used in the following analyses are all conditional on the WIG index being in its neutral phase. As noted above, westward disturbances are evident across the region and often occur concurrently with Kelvin waves. However, as we aim to first understand the modulation of local convection by Kelvin waves, we select for periods when WIG waves are not present for this study. That being said, future work exploring the relationship between these WIG disturbances and the subsequent impacts on MCS development would be beneficial.

Kelvin wave activity at T3, represented here as the percent of occurrence of olrkel $< -1.5\sigma$, or the percent occurrence of the active phase during each month, is shown in Fig. 3. The activity during the 2014–15 GOAmazon time period is overall consistent with the long-term climatology over the region, with March (wet season) and November (wet-to-dry transition) having the most activity, while June–September (dry season) have the least amount of activity, similar to the results shown in Liebmann et al. (2009). While the 2014–15 wet season (December–April) experienced overall normal Kelvin activity, January and April saw below normal wave activity, while March saw above normal activity. The 2014–15 dry season (July–September) was below normal, primarily due to a lack of wave activity in August and September. The transition from dry to wet (October–November) was also below normal due to the absence of Kelvin waves in October of 2014–15.

Time series variables at T3 and the CHUVA sites, as well as the VARANAL data product, are composited for each phase of the Kelvin wave by first subtracting the first seasonal harmonic and full data period mean of each variable. The first seasonal harmonic for each variable is estimated using daily means of all available observations of that quantity, regardless of instrument or location (T3 or CHUVA site), to maximize the sample size. Composites of variables with respect to the neutral, active, and suppressed convective phases of the waves are then constructed by identifying the days when both twice-daily values of the Kelvin wave index are of the same phase. Composite means and standard deviations of the mean are based on the daily anomalies within each phase. Mean diurnal cycles are constructed for the phases of the Kelvin wave in a similar manner except that hourly, or the smallest time step available from the dataset if data have higher than hourly frequency, anomalies are composited rather than daily anomalies after the seasonal cycle has been removed. The conditioning of the Kelvin index on a lack of WIG activity, as well as the removal of the seasonal cycle from the variables prior to compositing by Kelvin wave phase, assures that the composite anomalies are capturing primarily Kelvin wave modulations of each parameter.

e. Column precipitable water vapor

The surface Global Navigation Satellite System (GNSS) PWV observations at the CHUVA sites are available from a distributed network maintained during GOAmazon by the Instituto Nacional de Pesquisas Espaciais (INPE), Brazil, several of which were installed for the Amazon Dense GNSS Network in 2011 (Adams et al. 2015) (Fig. 1). While the AMF T3 site at Manacapuru provides information on the vertical structure of water vapor, surface temperature and moisture, and local precipitation, as well as detailed atmospheric boundary layer and cloud properties, the GNSS network provides information at high time resolution (5 min) on the regional variability of PWV, which is important for understanding the spatial extent of the modified convective environment on broader (5–100 km) spatial scales, similar to the SIPAM radar viewing region. The GNSS network also includes surface meteorological measurements with the exception of rainfall.

The GNSS 30-s data have been processed using GNSS-Inferred Positioning System and Orbit Analysis Simulation (GIPSY-OASIS) software with a cutoff elevation angle of 10° to obtain zenith total delay at 5-min intervals. This elevation angle results in an observation cone of approximately 10–15-km radius, capturing the spatial and temporal scales at which the shallow-to-deep convective transition occurs and upscale convective growth begins. Zenith total delay is then separated into its hydrostatic and wet delay components using 1-min in situ surface air temperature and pressure collected at the same location as the GNSS receiver. The zenith hydrostatic delay is estimated from surface pressure and latitude of the station using a well-known formulation (Bevis et al. 1992). The zenith wet delay is estimated from the surface temperature using the empirically derived relationship of Bevis et al. (1992). The estimated root-mean-square (rms) errors in the zenith wet delay using this method are 1%–2% (Bevis et al. 1992, 1994), resulting in 1%–2% estimated rms errors for the derived PWV. The GNSS receivers in the INPE network were limited to signals from GPS satellites. Thus, both GPS and GNSS are used interchangeably throughout this document.

The GNSS sites suffered occasional power outages during the GOAmazon period, and one site, MNUS, had a bad antenna

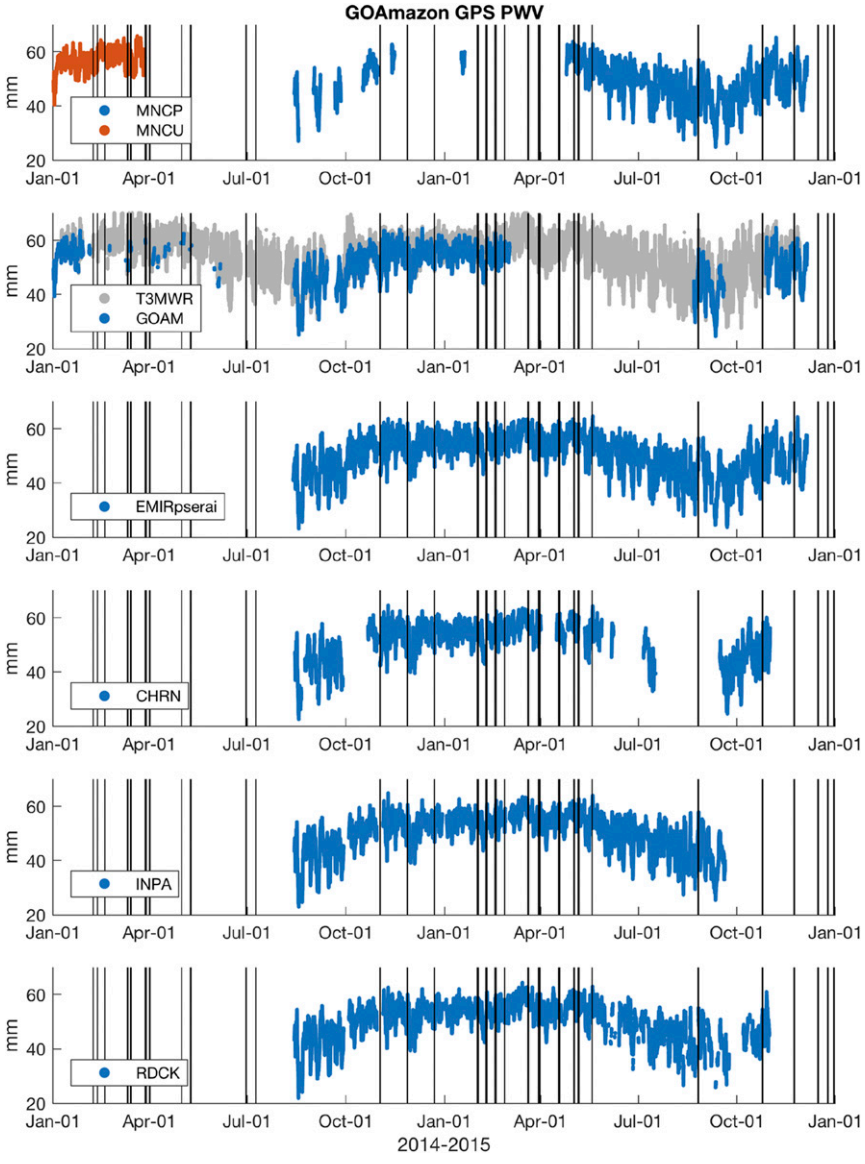

FIG. 4. Time series of GNSS PWV at seven sites (see Fig. 1 for locations) for the GOAmazon period. Also shown is MWR PWV at T3. As stated in the text, surface pressure from ERAI is used in the calculation of PWV at EMIR. Vertical black lines denote active Kelvin wave days defined using filtered OLR.

and was therefore unable to provide PWV throughout the entire experiment. However, as shown in Fig. 4, the remaining seven sites have several months of data both during active (vertical black lines in Fig. 4) and neutral Kelvin wave days. At EMIR, surface pressure data are of poor quality so ERAI 6-hourly surface pressure was linearly interpolated to this location and used to obtain PWV along with surface air temperature from the sensor at EMIR. Comparisons of the ERAI surface pressure at EMIR with nearby stations such as GOAM (40 km away) and a meteorological site 20 km away to the north along the Rio Negro show overall good agreement, although they are offset due to small altitude differences between the sites (not shown). The most apparent difference between the ERAI and observed surface pressure is in the diurnal cycle, with ERAI weaker in amplitude relative to the in situ pressure measurements (not shown). However, as this impacts all PWV at EMIR, comparisons of the different convective phases of the Kelvin wave on the diurnal cycle in PWV are still possible.

3. Kelvin wave activity over the Amazon

Figure 5 shows regressions of OLR and 200-hPa winds and streamfunction onto the Kelvin wave index from −4- to +2-day lags for the 2014–15 period following the methods described in section 2d above. At lag −4 days, a positive OLR anomaly (suppressed convection) is seen over the western Amazon, east

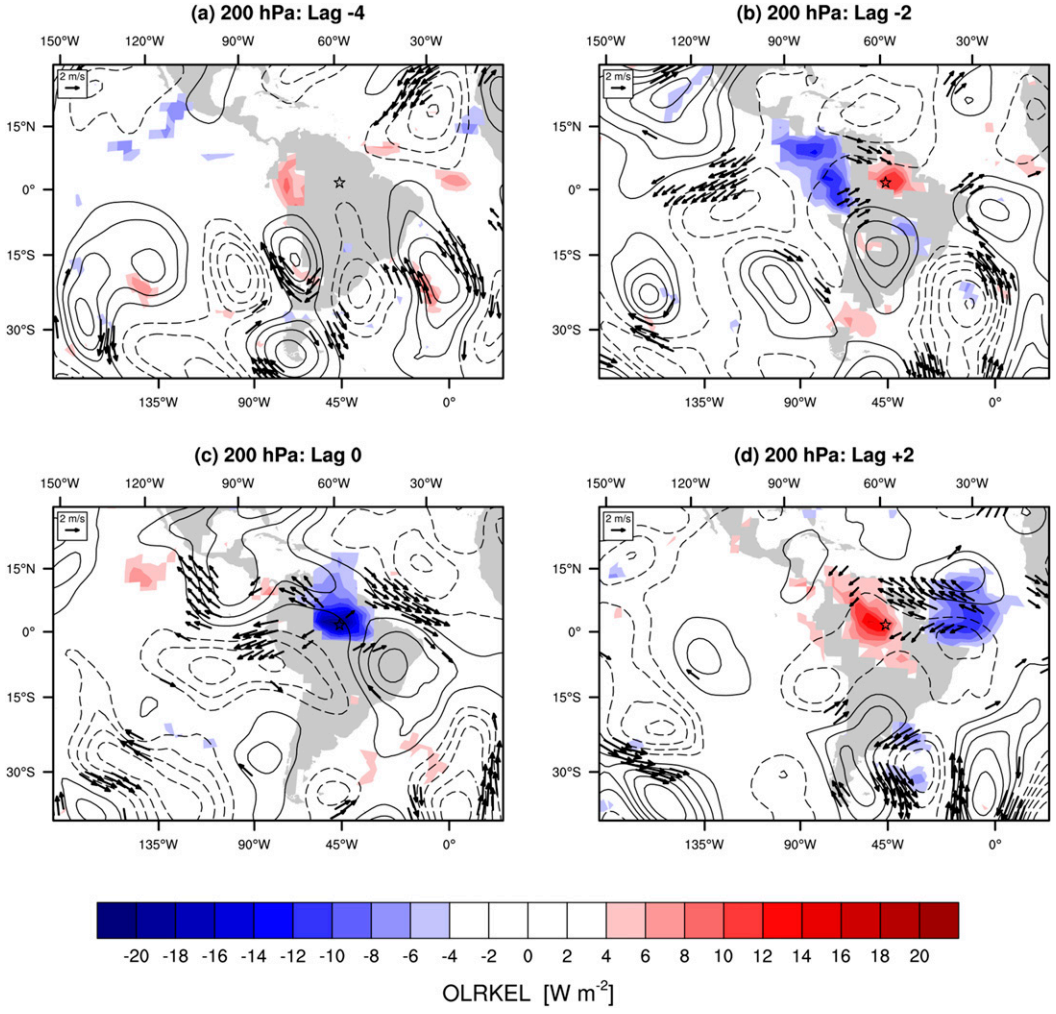

FIG. 5. Regressions of CDC OLR (shading) and ERAI 200-hPa wind vectors and streamfunction (contours) onto Kelvin-filtered OLR at T3 for the 2014–15 period. Only wind vectors and OLR regression amplitudes above the 90% confidence limit are plotted. A 2 m s^{-1} wind vector is shown at the top left of each panel. Streamfunction contours start at $\pm 7 \times 10^5$ m^2 s^{-1} and are plotted every 7×10^5 m^2 s^{-1}; negative contours are dashed. Every other wind vector is shown for readability. In all panels the location of T3 is indicated with a star.

of the Andes mountain range (Fig. 5a). The wind and streamfunction anomalies along 30°S suggest that Kelvin waves at T3 are associated with a precursor midlatitude disturbance propagating across southern South America from the South Pacific. This panel can be compared to Fig. 4a of Liebmann et al. (2009), where a midlatitude wave train is also seen a few days prior to the arrival of the Kelvin wave convective anomaly over the central Amazon. Liebmann et al. (2009) speculate that these midlatitude wave trains are associated with cold surges that propagate northward along the Andes at low levels and, if strong enough, can result in conditions that initiate Kelvin waves over equatorial South America.

Two days later the region of positive OLR anomalies moves east over T3, while a large region of negative OLR anomalies (enhanced deep convection) now appears over the western Amazon, northern Colombia, and tropical eastern Pacific (Fig. 5b). Easterly wind anomalies are observed in the equatorial eastern Pacific at this lag. By lag 0, the convective anomaly has shifted east over and to the north of T3 (Fig. 5c), moving out over the tropical Atlantic by lag +2 days (Fig. 5d), with a quadrupole of symmetric cyclones to the east and anticyclones to the west, suggesting a Rossby response to the Kelvin heating envelope. A positive OLR anomaly again develops over T3 at this time, indicating suppressed conditions have returned to the GOAmazon site.

Figure 6 is similar to Fig. 5 but for 850 hPa and shows regressions of geopotential heights instead of streamfunction, as the height anomalies better capture the wave horizontal structure at this level. At lag −4 days, a region of negative geopotential height anomalies is seen east of the Andes extending from the southern tip of South America to about 10°S (Fig. 6a). This feature is consistent with an equatorward elongation of a lee trough formed in association with the passage of an upper-level midlatitude wave train like that seen in

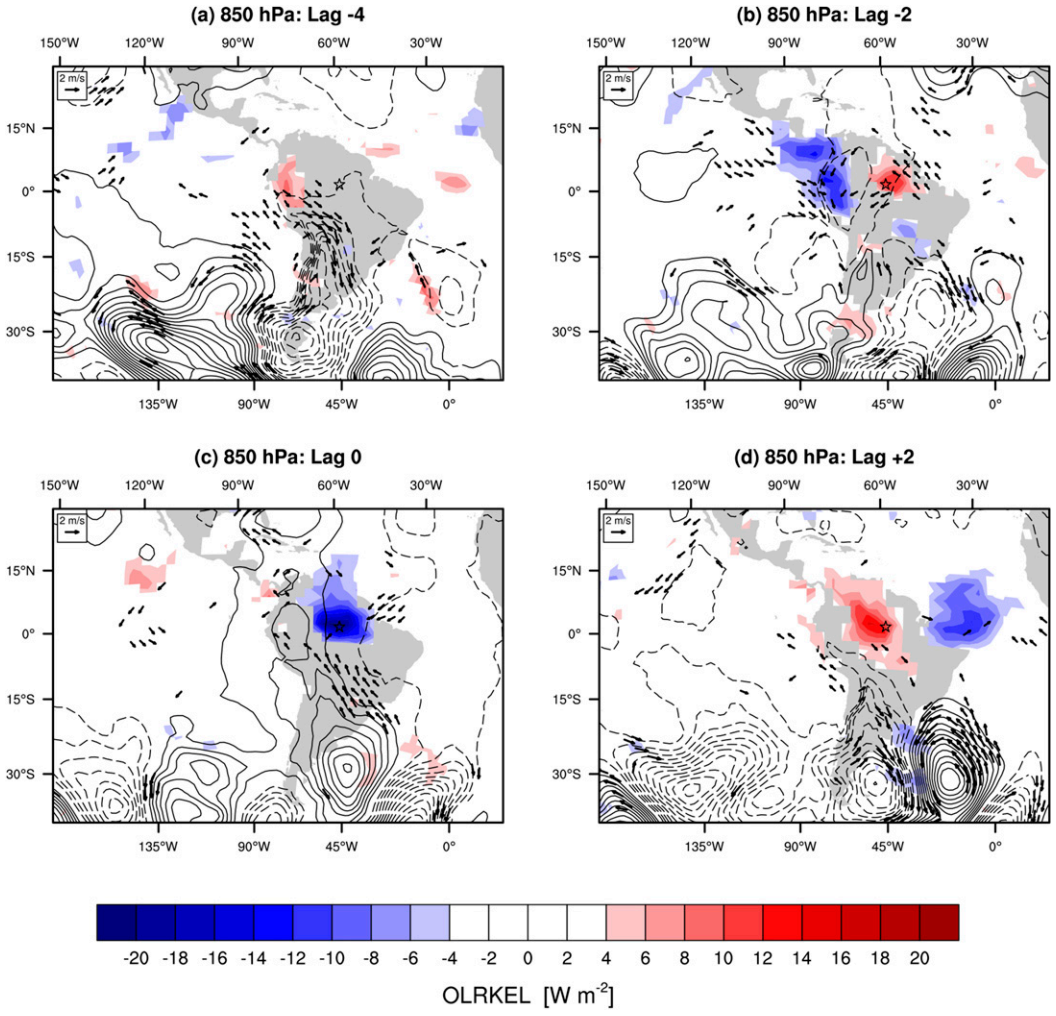

FIG. 6. As in Fig. 5, but for regressions of 850-hPa wind vectors and geopotential heights (contours), with height contours starting at ±2 m and plotted every 2 m.

Fig. 5a and as discussed in the literature on the austral summer transient circulations and South American monsoon variability (Garreaud and Wallace 1998; Vera et al. 2006). Northwesterly wind anomalies extend from the region of suppressed convection over the western Amazon southward along the east side of the Andes at low levels (Fig. 6a), suggesting a strengthening of the monsoon low-level circulation in association with the suppressed convection over the western Amazon. These low-level wind anomalies are accompanied by a corresponding increase in the vertically integrated moisture flux toward higher latitudes (Fig. 7a).

At lag −2 days, weak positive vertically integrated moisture flux divergence anomalies are evident around T3, while weak negative vertically integrated moisture flux divergence anomalies are seen over the western Amazon (Fig. 7b), corresponding to the regions of suppressed and active convection, respectively (Fig. 6b). At lag 0, southeasterly wind anomalies are seen across central South America and extending into the southwestern Amazon (Fig. 6c). To the east of T3, anomalous northeasterly flow converges along the coast of tropical South America. In contrast to lag −4, southeasterly low-level wind anomalies along the east side of the Andes indicate a weakening of the monsoon winds flowing from the central Amazon into southern South America. These wind anomalies reduce the vertically integrated moisture transport from the Amazon to higher latitudes and contribute to a broad region of negative vertically integrated moisture flux divergence anomalies extending southeasterly across the Central and southern Amazon (Fig. 7c) east of the climatological position of the SACZ (Vera et al. 2006). This anomalous moisture convergence provides favorable conditions for the enhanced convective activity observed at T3 at this time (Fig. 6c).

While previous studies have pointed out the links between tropical Pacific Kelvin waves and South American midlatitude disturbances and Kelvin waves observed over the central Amazon (Liebmann et al. 2009), as well as links between the midlatitude disturbances over southern South America and variability in the SACZ and SALLJ (Garreaud and Wallace 1998),

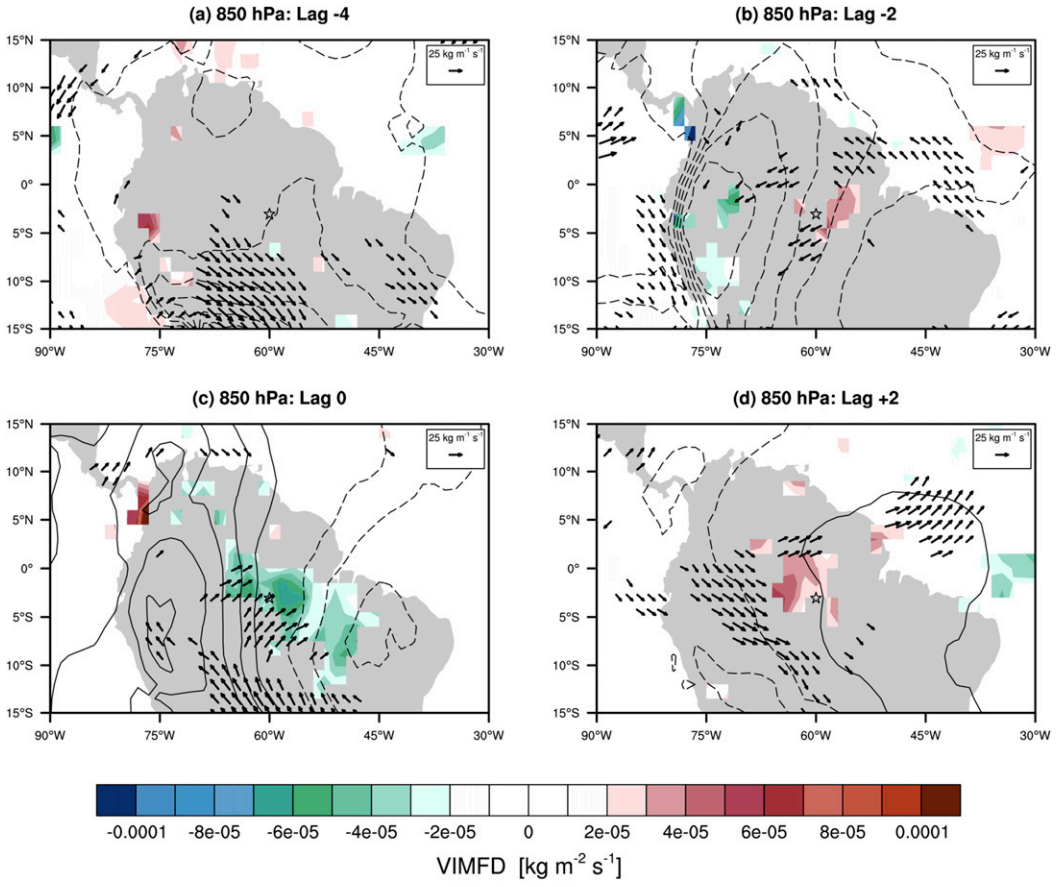

FIG. 7. As in Fig. 6, but for vertically integrated moisture flux (vectors) and moisture flux divergence (shading). A 25 kg m^{-1} s^{-1} moisture flux vector is shown in the top right of each panel. Geopotential height contours start at ±1 m and have an interval of 1 m. Only moisture flux vectors above the 90% confidence level and vertically integrated moisture flux divergence regressions above the 80% confidence level are shown.

here we highlight that once the wave is formed over the western Amazon, a consistent picture emerges regarding the anomalies in moisture flux and moisture flux divergence that accompany the Kelvin wave active and suppressed centers as they propagate east across the Amazon. Given the importance of integrated moisture to rainfall in the tropics, we hypothesize that these modulations in moisture flux, both along the east side of the Andes as well as the equatorial Atlantic coast, are an important mechanism linking Kelvin waves to localized development of convection over the central Amazon.

Figure 8 shows the ERAI surface heat flux component means and regressions at T3. The sign convention in Fig. 8a of this figure is such that positive (negative) values indicate heating (cooling) of the surface. Similarly, in Fig. 8b a positive (negative) anomaly corresponds to more (less) heating of the surface. The net surface flux in the region over the GOAmazon period is in approximate balance, with solar radiative heating balanced primarily by latent cooling. The increased widespread convection at T3 at the peak of Kelvin wave convective anomalies at lag 0 results in anomalous net cooling at the surface (red bar, Fig. 8b). This cooling is mainly due to a large reduction in net surface solar radiative heating, despite corresponding reductions in heat loss due to the surface longwave, sensible, and latent cooling terms. Following the peak convection at T3, the net surface heat flux anomaly returns to positive at lag +2 days (solid blue bars in Fig. 8). At this time, the longwave cooling anomalies are considerably less than those at lag −2 days (hatched blue bars) and shortwave heating is also less than at lag −2 days. These radiative flux anomalies imply that cloud cover at T3 is somewhat greater following the peak Kelvin wave convective activity than preceding it. This is in fact what is observed, as will be discussed in section 5 below.

Sensible cooling in ERAI is larger at lag −2 and +2 days than at lag 0, with more cooling at lag +2 than lag −2 days (Fig. 8). Further investigation reveals that neutral skin temperature anomalies are seen in ERAI at lag −2 while positive skin temperature anomalies appear at lag +2 (not shown), suggesting that stronger near surface temperature gradients likely contributed to the larger sensible cooling at lag +2. A similar result is seen for the latent heat fluxes but with smaller latent cooling anomalies for lag +2 days than at lag −2 days. The reduced latent cooling anomalies at lag +2 days in ERAI are consistent with small positive boundary layer relative humidity anomalies at T3 following the convectively active

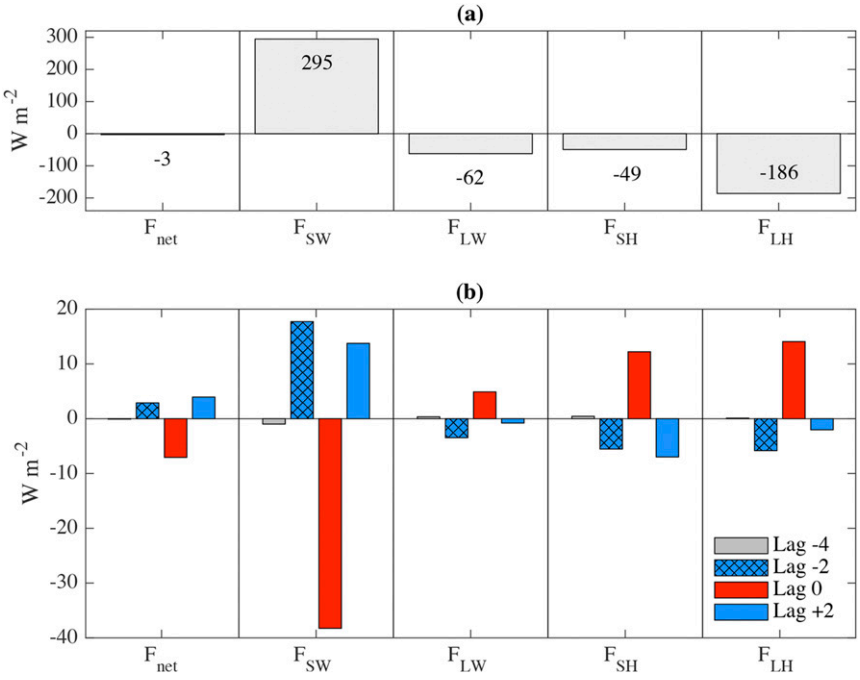

FIG. 8. ERAI (a) means and (b) regressions onto Kelvin-filtered OLR of net surface heat flux (F_{net}), net shortwave heat flux (F_{SW}), net longwave heat flux (F_{LW}), sensible heat flux (F_{SH}), and latent heat flux (F_{LH}) interpolated to T3 grid point. In (b) bars represent different lag in days with blue (red) bars indicating when suppressed (active) Kelvin wave convective anomalies are observed at T3.

Kelvin phase (not shown), driving reduced moisture fluxes locally. Evidence of advected moisture impacting local moisture fluxes has recently been shown (Welty et al. 2020).

4. Local modification of the environment by Kelvin waves

In the previous section we show that there is a modulation of the integrated water vapor flux and integrated moisture flux divergence over the region due to Kelvin waves, with active (suppressed) convective periods having a reduction (enhancement) in the southward moisture flux to mid latitudes. We also show that Kelvin waves impact the net surface heating at T3 through both modulation of the cloud radiative forcing, as well as through impacts on near surface thermodynamic quantities, which impact the surface sensible and latent heat fluxes. In this section, we take a closer look at wave modifications of the large-scale moisture flux and surface heating impact localized forcing on convection using observations at T3 and the GPS PWV network.

Figure 9 shows the modulation of rainfall at T3 by the waves for four different rainfall instruments at the AMF, composited following the method outlined in section 2d. These instruments all capture a similar pattern in daily averaged rain rate anomalies for the different phases of the Kelvin wave. In particular, the convectively active Kelvin period is characterized by higher daily rain rates than either the convectively neutral or suppressed periods, indicating significant modulation of rainfall at T3 due to the wave passage.

The regional PWV is also modulated by Kelvin waves (Fig. 10a), with enhanced column moisture during the convectively active phase compared to the suppressed phase. The moistening during the convectively active Kelvin phase is shown to fall in the 1–3-mm range across the GNSS network, corresponding to about half that of the total wet season anomaly of about 5 mm (Fig. 10b). These results reflect the now well-documented correlation between column water vapor

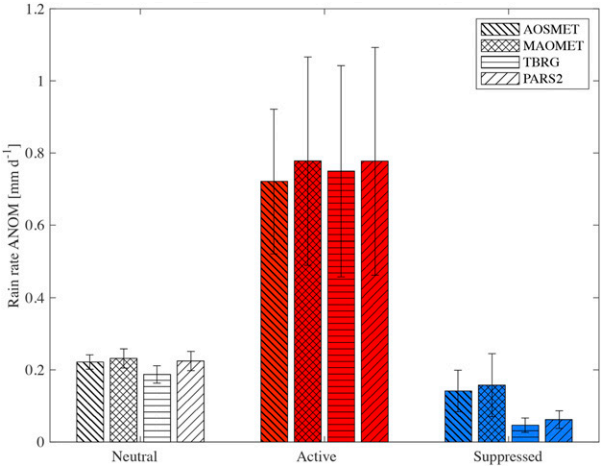

FIG. 9. Rain rate anomalies for convectively neutral, active, and suppressed Kelvin phase at Manacapuru (T3).

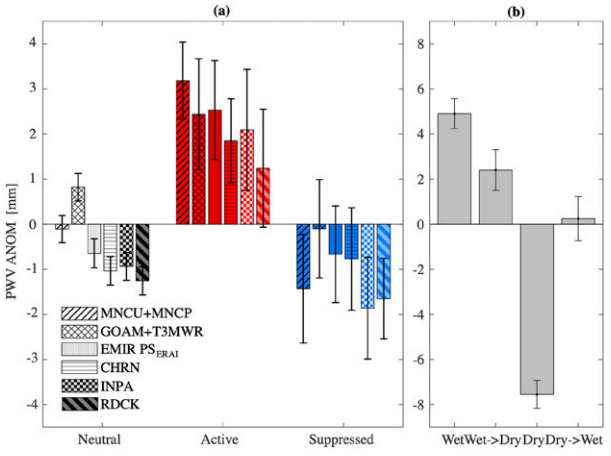

FIG. 10. PWV anomalies with respect to (a) convectively neutral, active, and suppressed Kelvin phase keyed on T3 and (b) the four seasons as defined in the text. In (a) PWV at MNCU is combined with PWV at MNCP, and PWV from the GPS at GOAM is combined with PWV from the MWR at T3 for this analysis. PWV at EMIR was obtained using surface pressure from ERAI. Note that the range of values for the seasonal anomalies is twice that of the Kelvin wave anomalies.

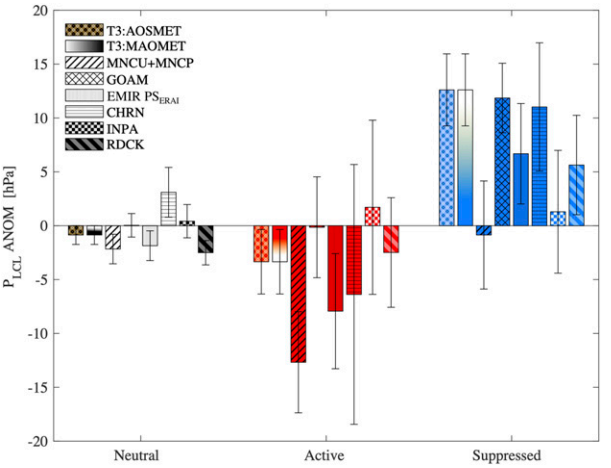

FIG. 11. As in Fig. 10a, but for P_{LCL} and using surface data from the GPS-met network except for at EMIR where surface pressure is provided by ERAI.

and rainfall in the tropics over both ocean and land areas (Bretherton et al. 2004; Holloway and Neelin 2009, 2010; Neelin et al. 2009; Muller et al. 2009; Adams et al. 2011, 2015, 2017; Kuo et al. 2017). The enhanced PWV over the GPS network also validates the ERAI integrated water vapor divergence patterns in Fig. 7, showing regional-scale PWV convergence (divergence) anomalies for the convectively active (suppressed) phase of the waves.

Increases in PWV over this region have been shown to contribute primarily to free-tropospheric moisture and reduced stability of the atmosphere, facilitating deep convection (Schiro et al. 2016, 2018; Kuo et al. 2017). This relationship is evidenced here by lower lifting condensation levels across the region (Fig. 11), represented as the pressure height from the surface to the lifting condensation level P_{LCL} (Betts et al. 2002). Increased moisture from 875 to 500 hPa is also evident for the convectively active phase of the Kelvin wave in both the radiosonde profiles at T3 and VARANAL product, representing the larger SIPAM radar domain (Fig. 12a). The increased moisture in the mid troposphere due to the Kelvin wave is about half that of the seasonal amplitude in moisture anomalies during the wet season (green lines in Fig. 12a), highlighting that a large fraction of the differences in PWV during the convectively active phase shown in Fig. 10a are due to moisture convergence above the boundary layer. The radiosonde data also suggest the convectively active Kelvin wave phase (and wet season) has increased boundary layer moisture below about 975 hPa not seen in the VARANAL product. As noted in the previous section, this low-level moisture tends to persist in the days following the convectively active phase of the wave (not shown). The peak moisture anomaly at about 650 hPa lies just above the level of peak convergence in the column over the SIPAM radar domain during the convectively active period in the VARANAL product (Fig. 12b) and is also consistent with the ERAI integrated moisture convergence anomalies shown in Fig. 7c across this same domain.

Composites of the apparent heating due to diabatic processes are shown in Fig. 12c. The peak anomalies in diabatic heating in VARANAL are broadly positive above 800 hPa, suggestive of the lifted heating profiles of MCSs with broad stratiform regions (Schumacher et al. 2004). Thus, the enhanced free-tropospheric moisture, low-level mass convergence, and reduced stability associated with the Kelvin convectively active period is contributing to the latent heating of the mid troposphere through the development of organized convection. This can be contrasted with the convectively suppressed phase of the wave, when diabatic heating anomalies are significantly less than during the active phase, except in the lower troposphere. The overall smaller magnitude and lower level of peak heating anomalies in the Kelvin-suppressed-phase Q_1 profile suggest a greater contribution from shallow or nonprecipitating convection during this phase of the wave (Schumacher et al. 2004; Tang et al. 2016). The Q_1 profile for the neutral period has a peak at 750 hPa and anomalies are larger overall above 875 hPa than in the convectively suppressed phase, suggesting neutral periods, mostly representative of the dry season, are dominated by isolated deep convection (Schumacher et al. 2004). The larger Q_1 anomalies during the neutral periods compared to the convectively suppressed periods of the waves are consistent with the neutral boundary layer and neutral to slightly divergent free troposphere for these cases, while the convectively suppressed cases show a divergent boundary layer and slightly convergent free troposphere, both unfavorable to deep convection and MCS formation (Fig. 12b). In the next section we explore the nature of the organization of convection during the different phases of the Kelvin wave and the resulting impacts on the diurnal cycle of convection.

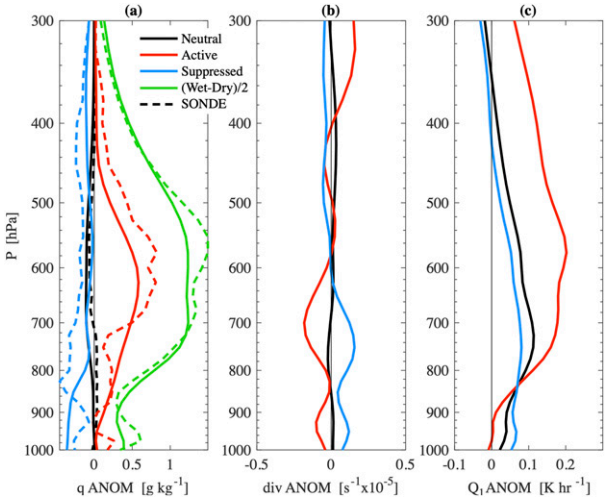

FIG. 12. (a) Anomalies of specific humidity from radiosonde at T3 (dashed) and VARANAL (solid) with respect to GOAmazon period for the convectively neutral, active, and suppressed phases of the Kelvin wave keyed on T3. Profiles of (b) divergence and (c) Q_1 from the VARANAL product also shown. The amplitude of the seasonal cycle in specific humidity is shown for comparison in (a). Legend is applicable to all panels.

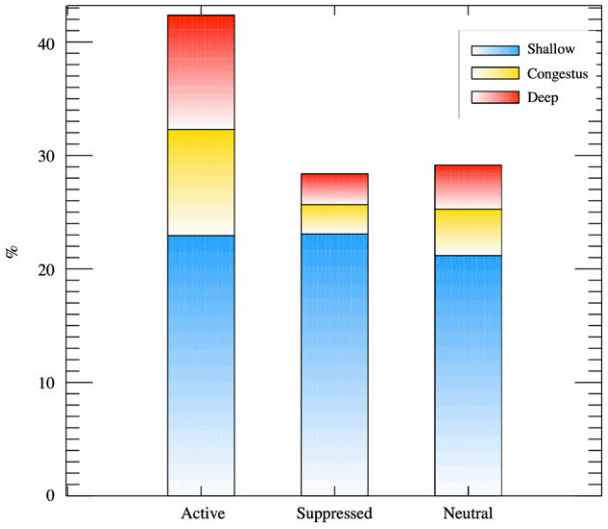

FIG. 13. Cloud-type occurrence relative to all available cloud profiles from the Merged Cloud Mask and Cloud Type data product separated into deep, congestus, and shallow convection and by Kelvin wave convective phase.

5. Modulation of the shallow to deep transition by Kelvin waves

The occurrence of convection at T3 is evaluated using the Merged Cloud Mask and Cloud Type data product described in section 2a. At a given time, the occurrence of different cloud types is documented within a vertical column, with cloud-type definitions based on cloud boundaries and thickness. Convection is divided into shallow (cloud-base height < 3 km, cloud-top height < 3 km), congestus (cloud-base height < 3 km, cloud-top height 3–8 km, cloud thickness > 1.5 km), and deep (cloud-base height < 3 km, cloud-top height > 8 km, cloud thickness > 5 km). Figure 13 shows the occurrence of these individual categories with respect to the total number of cloud profiles available, further categorized by Kelvin wave phase. As expected, convection is overall most frequent during the convectively active Kelvin wave phases, followed by neutral, and then suppressed convective phases. Deep convection, in particular, is more prevalent at T3 during the convectively active phase followed by the neutral phase, consistent with the higher rain rates observed at T3 during these phases and the magnitude and shape of the heating profiles for these phases relative to the convectively suppressed phase (section 4).

While these composites show that deep convection and heavy rainfall occur more frequently over T3 during the convectively active wave phase, it is not clear from this analysis alone how the timing of the convection corresponds to the increase in PWV, also associated with the active phase. To investigate this relationship further, Fig. 14 shows the diurnal cycle in PWV (top panel), along with the large-scale rainfall over the SIPAM domain (bottom panel), for convectively active, suppressed, and neutral wave phases. The bottom panel also shows the diurnal cycle in surface temperature based on all PWV sites as a reference, with the diurnal cycle repeated for each day. In all panels the day prior and following the Kelvin classification on day 0 is shown to better understand the local modulation of convective development on synoptic time scales. As noted in section 2d, day 0 are days when all Kelvin wave OLR anomalies satisfy the conditions defining the convective wave phase.

Focusing on the neutral curve, PWV generally increases with the onset of peaks in the diurnal cycle of rainfall, with the peak in PWV slightly leading the peak in rainfall thought to represent the local convergence of water vapor associated with the local convection (Adams et al. 2011, 2013). During the active phase on day 0, PWV is seen to increase well ahead of the peak in rainfall suggesting a moistening of the troposphere over several hours prior to the onset of deep convection. PWV has been shown to peak prior to the onset of heavy rain in association with mesoscale circulations in the tropics (Holloway and Neelin 2010). Yasunaga and Mapes (2012) assert that Kelvin waves, along with other divergent wave types, exhibit this type of phase relationship between PWV and rainfall because MCSs dominate the convection coupled to this category of convectively coupled waves. These authors argue that MCSs tend to grow and organize in moist environments, resulting in PWV leading rainfall in these regimes. In contrast, in isolated deep convective environments convection tends to moisten the environment and PWV lags rainfall. Such a phase relationship would be difficult to see here as we have not focused on compositing isolated deep convective cases for this analysis. The moistening during the active phase is seen to continue into day +1, with daytime PWV significantly higher than observed for suppressed days. Suppressed days show an overall drying beginning on day 0 and continuing through day +1.

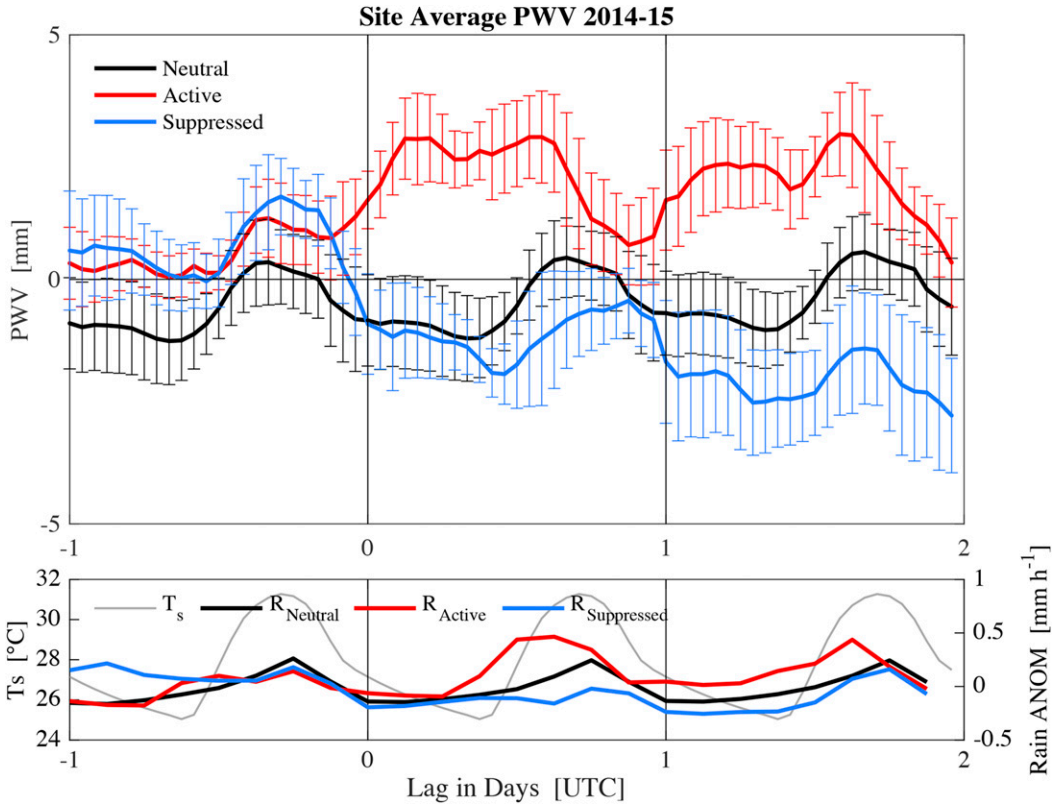

FIG. 14. (top) Site hourly averaged PWV anomalies shown over the diurnal cycle centered on day 0 (0000 UTC of day when wave is in the indicated phase) for the convectively neutral, active, and suppressed phases of the wave. Day −1 and day +1 are also shown. Error bars denote the standard deviation of the mean of the sites. (bottom) Site hourly average surface temperature for diurnal solar heating reference along with the 3-hourly VARANAL large-scale rain-rate anomalies by Kelvin wave convective phase. All shown over the diurnal cycle centered on day 0, as in the top panel.

A similar plot for the convective and deep convective cloud-type categories shows the more frequent occurrence of convection, especially deep convection, during the convectively active phases and reduced convective activity during suppressed phases (Fig. 15). The data plotted are the average cloud fraction for convection (left) and deep convection (right) for periods associated with the Kelvin wave phases for each hour of day 0 (starting at 0000 UTC, denoted as lag 0) and day ±1, as in Fig. 14. The highest convective cloud fractions overall occur in the lowest levels, reflective of the frequent shallow convection in all phases. Convection makes up a small fraction of clouds during day 0 of the convectively suppressed phase and is confined primarily to the afternoon and evening during the neutral phase, suggesting the dominance of diurnally forced convection when not under the influence of Kelvin waves. Focusing solely on deep convection, we see that deep convection at T3 can occur throughout the entire day that is under the influence of the convectively active phase of the Kelvin wave. Overnight (day 0 into +1) deep convection is not seen in the other phases, which have some afternoon deep convection, more so for the diurnally forced neutral Kelvin wave phase and less so for the suppressed day 0, consistent with the Q_1 profiles in Fig. 12. In both the convectively active and suppressed panels, day −1 and day +1 can feature afternoon deep convection.

The SIPAM radar data provide the broader context of these convective systems at T3 through analysis of precipitating features across a 100 km × 100 km domain covering T3 and the GPS sites. Kelvin wave composites of rainfall over the SIPAM domain (Fig. 16a) show overall more rainfall during the convectively active Kelvin wave phase, similar to what is observed at T3 (Fig. 9), with the least amount of rainfall occurring during the suppressed phase. Most of the Kelvin wave activity occurs during the wet season, where the difference between convectively active and suppressed Kelvin wave SIPAM rainfall is on the same order as the difference in accumulated rainfall between the wet and the dry seasons (Fig. 16b). When considering only the rain produced by features meeting the 100-km major-axis MCS criteria (Fig. 16a), while there is rainfall from MCSs in all Kelvin wave convective phases, most occurs in the active phase, supporting the results of Yasunaga and Mapes (2012).

It was surprising to see nearly 1000 mm of rain from MCSs during the suppressed phase. Closer analysis of individual cases revealed that this total came from one event during March 2014 (wet season) when a long-lived MCS moved into the SIPAM domain from the east on the previous day, persisting into the

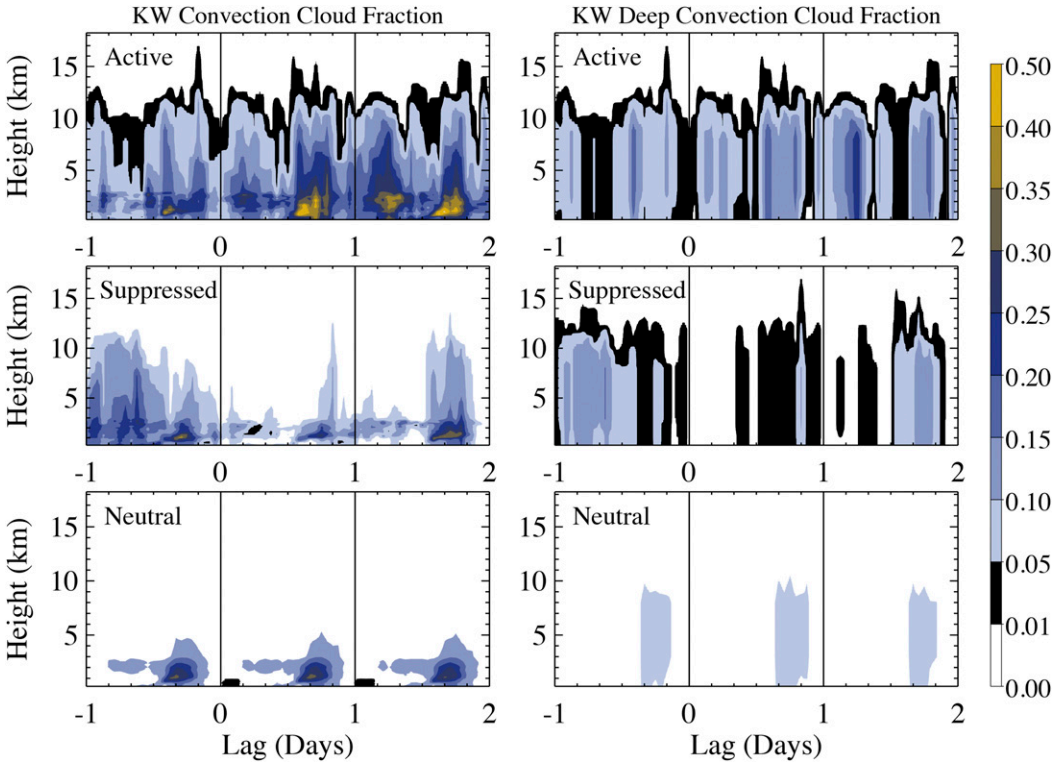

FIG. 15. Average cloud fraction from the Merged Cloud Mask and Cloud Type data product for (left) all convective categories and (right) deep convection only for the convectively (top) active, (middle) suppressed, and (bottom) neutral Kelvin wave phases. Day 0 represents 0000 UTC on the day of the wave convectively active phase (minor tick marks every 4 h; LT = UTC − 4 h) with day −1 and +1 also plotted.

next day characterized by a suppressed Kelvin wave phase. However, MCSs during the suppressed phase were rare, especially compared to the convectively active Kelvin phases, with only 2 of the 25 days influenced by the suppressed Kelvin wave phase (and with continuous SIPAM data coverage throughout the day) compared to 7 out of the 19 convectively active days having radar precipitation features identified as MCSs.

The diurnal analysis of the SIPAM precipitating features is presented in Fig. 17 for the convectively active, suppressed, and neutral Kelvin days with lag 0 as defined in Figs. 14 and 15. Figure 17a provides a count of the number of sub-MCS features (e.g., major axis < 100 km) identified in the SIPAM domain, normalized by the total number of scans in that Kelvin convective phase category. A strong diurnal cycle is illustrated for all Kelvin wave convective phases, with most of the smaller (i.e., sub-MCS) precipitating features occurring in the afternoon with no statistically significant (at the 95% confidence interval) differences between phases in the number of sub-MCSs occurring during the afternoon and evening. Previous work has shown that the diurnal cycle of precipitation in this region is influenced by local circulations driven by the topography (including rivers) around Manaus (e.g., Cohen et al. 2014; dos Santos et al. 2014) with an afternoon peak in deep convection associated with the inland propagation of the seabreeze front and local river circulations (e.g., Burleyson et al. 2016). During the wet season, when the atmosphere is moister, a higher occurrence of shallow convection reduces solar radiation to the surface and delays the shallow-to-deep convective transition (Zhuang et al. 2017). Here, we see that the increased moisture in the morning observed on day −1 of the Kelvin convectively suppressed phase (e.g., Fig. 14) is associated with a delay in timing of isolated deep convection on day 0 (Figs. 14, 15, and 17a) compared to the neutral Kelvin wave phase, the latter of which occurs throughout the wet, dry, and transitional seasons. During the convectively active Kelvin wave phase, when a higher portion of rainfall comes from MCSs compared to other phases (Fig. 16) and can lead to differences in the phase of the diurnal cycle (e.g., Adams et al. 2013; Burleyson et al. 2016), the afternoon peak in sub-MCSs occurs earlier (Fig. 17a). There is also a noticeable and statistically significant difference between convectively active and suppressed Kelvin wave phases in the overnight and morning hours, with sub-MCS features present in greater numbers for convectively active phases, similar to the more frequent occurrence of deep convection at T3 during active periods during all times of day. These differences are more pronounced when focusing on the MCS features, with the percentage of the SIPAM domain covered by MCS grid points displayed (Fig. 17b), especially with the prolonged occurrence of MCSs during convectively active phases later into the night and into the next day (day +1). The spread is large, however, as the sample size of MCSs is relatively small during these phases

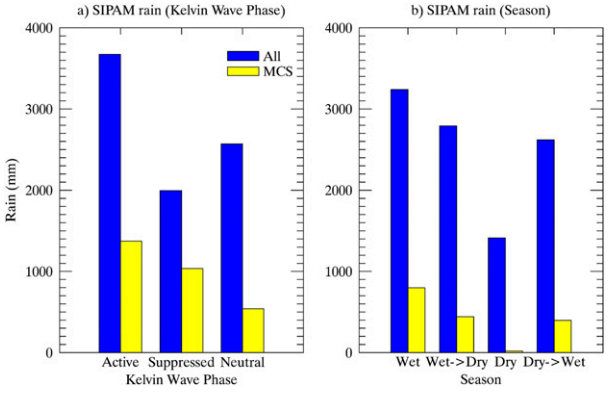

FIG. 16. Total volume rain over the 100 km × 100 km gridded SIPAM domain, derived from reflectivity and normalized by the total number of scans in each wave convective phase. (a) Divided by Kelvin wave phase for the entire GOAmazon period and (b) for each season (wet, wet to dry, dry, dry to wet) regardless of Kelvin wave phase.

(7 out of 19 active days experiencing MCSs) and the peak timing of these MCS active phase events vary. These results can be compared to those over the tropical Indian Ocean, where Kelvin wave activity was shown to control the timing of deep convective systems during convectively active periods of the Madden–Julian oscillation (MJO), whereas the diurnal cycle dominated the relatively drier suppressed MJO periods when no synoptic-scale wave activity was observed (Rowe et al. 2019). Overall, the SIPAM analysis supports the conclusion that MCSs are more frequently observed during convectively active phases of the Kelvin wave when lifting condensation levels are lower and PWV is increased compared to the suppressed and neutral Kelvin wave convective phases.

6. Discussion and conclusions

This study aims to improve understanding of the local and large-scale controls on convective development over the central Amazon through use of data collected during the GOAmazon 2014–15 and CHUVA field campaigns. We approach this knowledge gap through a focus on Kelvin waves, which have previously been identified over the central Amazon primarily during the wet season (Liebmann et al. 2009). The present study finds that Kelvin waves during GOAmazon exhibit important forcings on the large-scale dynamic and thermodynamic fields that impact localized convective development. In particular, during the convectively suppressed phase of the waves, the low-level circulation is strongly modulated by Kelvin waves and is coincident with regions of anomalous moisture flux along the Atlantic coast and western Amazon, corresponding to enhanced moisture flux divergence over the central Amazon. During the convectively active phase of the waves, reduced southeastward moisture flux along the east side of the Andes results in anomalous low-level moisture convergence over the central Amazon.

Strong modulation of radiative, sensible, and latent heat fluxes is also observed in response to Kelvin wave activity. During the convectively suppressed phase of the waves, both enhanced radiative heating as well as enhanced longwave, sensible, and latent cooling of the surface are observed. However, the surface fluxes show asymmetries in time about the convectively active phase. The moisture fluxes in particular show enhanced cooling 2 days prior to the arrival of the convectively active phase but show reduced anomalies 2 days following this phase. The enhanced low-level moisture associated with the convectively active phase persists following the peak activity and is thought to reduce the surface moisture fluxes at this time. A similar pattern is seen in longwave cooling. In this case, persistent low clouds following the convectively active phase are thought to reduce the radiative cooling of the surface on the days following this phase.

A closer look at T3 through GOAmazon/CHUVA ground-based instruments shows that the convectively active Kelvin phase is characterized by higher average rain rates than the convectively neutral or suppressed phases, indicating a significant modulation of rainfall due to the wave passage. This increase in rainfall during convectively active phases follows a broader regional increase in PWV seen across the GNSS network, with enhanced column moisture observed during the active phase and reduced column moisture during the suppressed phase. In addition, lower lifting condensation levels are observed across the region during the convectively active phase than during the neutral and suppressed phases. Enhanced moisture and reduced stability associated with the Kelvin wave convectively active phase contributes to the latent heating of the mid- to upper troposphere through the development of organized convection. Indeed, deep convection at T3 is more frequent and occurs at more times throughout the day during the convectively active phase compared to the suppressed and neutral phases, with the least amount of deep convection at T3 occurring during convectively suppressed phases. Scanning radar data show that rainfall increases across this broader domain encompassing T3 corresponding to the enhanced PWV during the convectively active phases. A radar-based precipitation feature analysis shows that this enhancement in rainfall across the radar domain is largely associated with an increase in MCS activity during this phase. The most statistically significant difference in MCS coverage between the wave convective phases occurred in the overnight and early morning hours as MCSs persisted into day +1 for convectively active phases, whereas local diurnally forced convection is observed for the convectively neutral phase and convection is overall reduced, especially organized systems, during the suppressed phase.

There is, however, an exception when a persistent MCS influenced the broader GOAmazon domain within a suppressed Kelvin wave phase. This appeared to be an isolated case and shows that while MCSs can occur outside of a convectively active Kelvin wave phase (55 out of nearly 400 neutral days during GOAmazon had MCS-scale features), MCSs are more prevalent under the favorable environmental conditions provided by the convectively active wave phase. We aim to further explore the relationship between MCS development

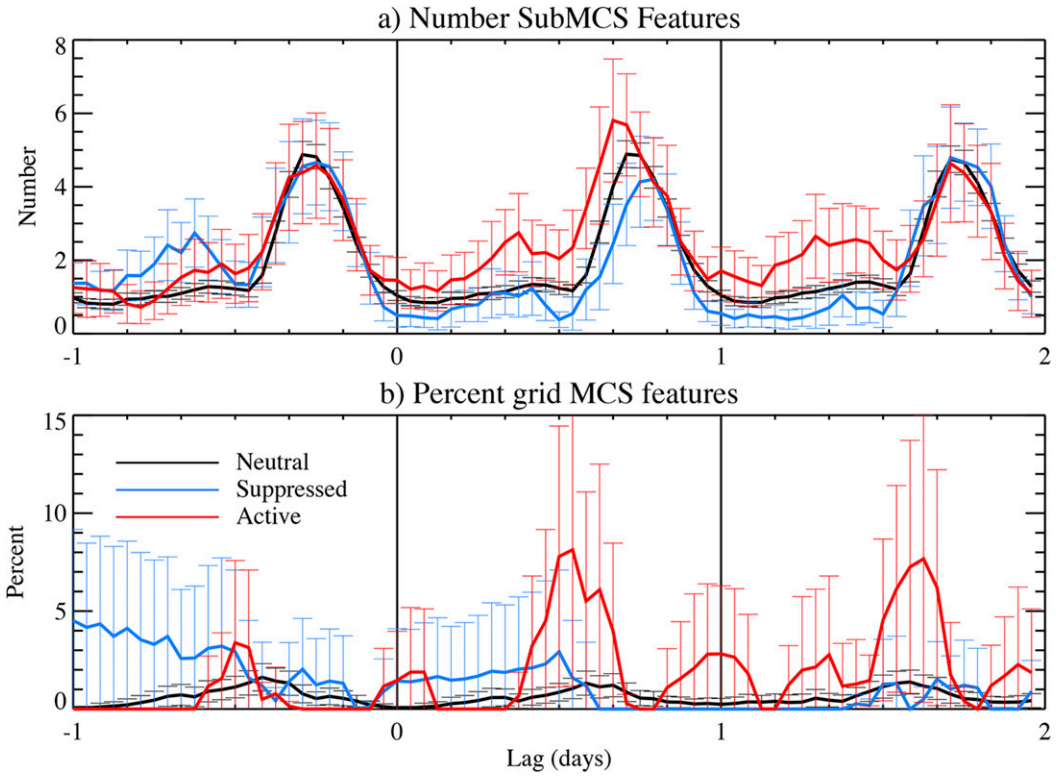

FIG. 17. Time series of the precipitation feature analysis from the SIPAM domain. (a) The number of sub-MCS features as a function of hour relative to the day of the wave convective phase occurrence for each Kelvin wave phase. The total number for each wave category is normalized by the total number of scans for that phase. (b) The percentage of the SIPAM grid covered by MCS-identified grid points for all SIPAM files on days characterized by the corresponding Kelvin wave convective phase. Error bars in both plots represent the 95% confidence interval. Lag day 0 corresponds to 0000 UTC on the day of the Kelvin wave convective phase (minor tick marks every 4 h; LT = UTC − 4 h).

and Kelvin waves through high-resolution model runs in a follow-up study. Furthermore, additional large-scale influences, such as WIG waves, which are intentionally excluded from this analysis, can be explored to determine additional controls on local convection in the central Amazon.

Acknowledgments. We thank Henrique Barbosa, Ludmila Silva, Bruno Takeshi, Luiz A. T. Machado, and Luiz F. Sapucci for their assistance with obtaining the GPS-Met data used in this analysis. We also thank Dr. Alice Grimm and two anonymous reviewers who greatly improved the clarity and quality of this manuscript over the original. This work is supported through DOE ASR Grant DE-SC0016222. This publication is partially funded by the Joint Institute for the Study of the Atmosphere and Ocean (JISAO) under NOAA Cooperative Agreement NA15OAR4320063, Contribution 2020-1073. The T3 and SIPAM data are available from the ARM data archive (https://www.arm.gov/data), and the GPS-Met data are available from the CHUVA data server (http://chuvaproject.cptec.inpe.br) or by contacting Luiz Sapucci. ERAI data are available from the Copernicus Climate Change Service data server (https://www.ecmwf.int/en/forecasts/datasets/archive-datasets/reanalysis-datasets/era-interim). Kelvin wave identification, radar feature analysis, and GPS PWV are available from the authors by request.

REFERENCES

Adams, D. K., and Coauthors, 2011: A dense GNSS meteorological network for observing deep convection in the Amazon. *Atmos. Sci. Lett.*, **12**, 207–212, https://doi.org/10.1002/asl.312.

——, S. I. Gutman, K. L. Holub, and D. S. Pereira, 2013: GNSS observations of deep convective time scales in the Amazon. *Geophys. Res. Lett.*, **40**, 2818–2823, https://doi.org/10.1002/grl.50573.

——, and Coauthors, 2015: The Amazon dense GNSS meteorological network: A new approach for examining water vapor and deep convection interactions in the tropics. *Bull. Amer. Meteor. Soc.*, **96**, 2151–2165, https://doi.org/10.1175/BAMS-D-13-00171.1.

——, H. M. J. Barbosa, and K. P. Gaitán De Los Ríos, 2017: A spatiotemporal water vapor–deep convection correlation metric derived from the Amazon dense GNSS meteorological network. *Mon. Wea. Rev.*, **145**, 279–288, https://doi.org/10.1175/MWR-D-16-0140.1.

Alcântara, C. R., M. A. F. Silva-Dias, E. P. Souza, and J. C. P. Cohen, 2011: Verification of the role of the low level jets in Amazon squall lines. *Atmos. Res.*, **100**, 36–44, https://doi.org/10.1016/j.atmosres.2010.12.023.

Betts, A. K., J. D. Fuentes, M. Garstang, and J. H. Ball, 2002: Surface diurnal cycle and boundary layer structure over Rondônia during the rainy season. *J. Geophys. Res.*, **107**, 8065, https://doi.org/10.1029/2001JD000356.

——, G. Fisch, C. von Randow, M. A. F. Silva Dias, J. C. P. Cohen, R. da Silva, and D. R. Fitzjarrald, 2009: The Amazonian boundary layer and mesoscale circulations. *Amazonia and Global Change*, *Geophys. Monogr.*, Vol. 186, Amer. Geophys. Union, 163–181, https://doi.org/10.1029/2008GM000725.

Bevis, M., S. Businger, T. A. Herring, C. Rocken, R. A. Anthes, and R. H. Ware, 1992: GPS meteorology: Remote sensing of atmospheric water vapor using the global positioning system. *J. Geophys. Res.*, **97**, 15 787–15 801, https://doi.org/10.1029/92JD01517.

——, ——, S. Chiswell, T. A. Herring, R. A. Anthes, C. Rocken, and R. H. Ware, 1994: GPS meteorology: Mapping zenith wet delays onto precipitable water. *J. Appl. Meteor.*, **33**, 379–386, https://doi.org/10.1175/1520-0450(1994)033<0379:GMMZWD>2.0.CO;2.

Bretherton, C. S., M. E. Peters, and L. E. Back, 2004: Relationships between water vapor path and precipitation over the tropical oceans. *J. Climate*, **17**, 1517–1528, https://doi.org/10.1175/1520-0442(2004)017<1517:RBWVPA>2.0.CO;2.

Burleyson, C. D., C. N. Long, and J. M. Comstock, 2015: Quantifying diurnal cloud radiative effects by cloud type in the tropical western Pacific. *J. Appl. Meteor. Climatol.*, **54**, 1297–1312, https://doi.org/10.1175/JAMC-D-14-0288.1.

——, Z. Feng, S. M. Hagos, and J. Fast, 2016: Spatial variability of the background diurnal cycle of deep convection around the GoAmazon2014/5 field campaign sites. *J. Appl. Meteor. Climatol.*, **55**, 1579–1598, https://doi.org/10.1175/JAMC-D-15-0229.1.

Clothiaux, E. E., T. P. Ackerman, G. G. Mace, K. P. Moran, R. T. Mrachand, M. A. Miler, and B. E. Martner, 2000: Objective determination of cloud heights and radar reflectivities using a combination of active remote sensors at the ARM CART sites. *J. Appl. Meteor.*, **39**, 645–665, https://doi.org/10.1175/1520-0450(2000)039<0645:ODOCHA>2.0.CO;2.

Cohen, J. C. P., M. A. F. Silva Dias, and C. A. Nobre, 1995: Environmental conditions associated with Amazonian squall lines: A case study. *Mon. Wea. Rev.*, **123**, 3163–3174, https://doi.org/10.1175/1520-0493(1995)123<3163:ECAWAS>2.0.CO;2.

——, D. R. Fitzjarrald, F. A. F. D'Oliveira, I. Saraiva, I. R. da Silva Barbosa, A. W. Gandu, and P. A. Kuhn, 2014: Radar-observed spatial and temporal rainfall variability near the Tapajos-Amazon confluence. *Rev. Bras. Meteor.*, **29**, 23–30, https://doi.org/10.1590/0102-778620130058.

Dee, D. P., and Coauthors, 2011: The ERA-Interim reanalysis: Configuration and performance of the data assimilation system. *Quart. J. Roy. Meteor. Soc.*, **137**, 553–597, https://doi.org/10.1002/qj.828.

dos Santos, M. J., M. A. F. Silva Dias, and E. D. Freitas, 2014: Influence of local circulations on wind, moisture, and precipitation close to Manaus City, Amazon region, Brazil. *J. Geophys. Res. Atmos.*, **119**, 13 233–13 249, https://doi.org/10.1002/2014JD021969.

Dunkerton, T. J., and F. X. Crum, 1995: Eastward propagating ~2- to 15-day equatorial convection and its relation to the tropical intraseasonal oscillation. *J. Geophys. Res.*, **100**, 25 781–25 790, https://doi.org/10.1029/95JD02678.

Fan, J., and Coauthors, 2018: Substantial convection and precipitation enhancements by ultrafine aerosol particles. *Science*, **359**, 411–418, https://doi.org/10.1126/science.aan8461.

Feng, Z., and S. Giangrande, 2018: Merged RWP-WACR-ARSCL cloud mask and cloud type. ARM, accessed 11 April 2017, https://doi.org/10.5439/1462693.

Garreaud, R. D., and J. M. Wallace, 1998: Summertime incursions of midlatitude air into subtropical and tropical South America. *Mon. Wea. Rev.*, **126**, 2713–2733, https://doi.org/10.1175/1520-0493(1998)126<2713:SIOMAI>2.0.CO;2.

Giangrande, S. E., and Coauthors, 2017: Cloud characteristics, thermodynamic controls and radiative impacts during the observations and modeling of the Green Ocean Amazon (GoAmazon2014/5) experiment. *Atmos. Chem. Phys.*, **17**, 14 519–14 541, https://doi.org/10.5194/acp-17-14519-2017.

Gimeno, L., A. Stohl, R. M. Trigo, and F. Dominguez, 2012: Oceanic and terrestrial sources of continental precipitation. *Rev. Geophys.*, **50**, RG4003, https://doi.org/10.1029/2012RG000389.

Grimm, A. M., 2011: Interannual climate variability in South America: Impacts on seasonal precipitation, extreme events, and possible effects of climate change. *Stochastic Environ. Res. Risk Assess.*, **25**, 537–554, https://doi.org/10.1007/s00477-010-0420-1.

——, and M. A. F. Silva Dias, 2011: Synoptic and mesoscale processes in the South American monsoon. *The Global Monsoon System: Research and Forecast*, C. P. Chang et al., Eds., World Scientific Series on Asia-Pacific Weather and Climate, Vol. 5, World Scientific Publishing Company, 239–256, https://doi.org/10.1142/9789814343411_0014.

Holloway, C. E., and J. D. Neelin, 2009: Moisture vertical structure, column water vapor, and tropical deep convection. *J. Atmos. Sci.*, **66**, 1665–1683, https://doi.org/10.1175/2008JAS2806.1.

——, and ——, 2010: Temporal relations of column water vapor and tropical precipitation. *J. Atmos. Sci.*, **67**, 1091–1105, https://doi.org/10.1175/2009JAS3284.1.

Kiladis, G. N., M. C. Wheeler, P. T. Haertel, K. H. Straub, and P. E. Roundy, 2009: Convectively coupled equatorial waves. *Rev. Geophys.*, **47**, RG2003, https://doi.org/10.1029/2008RG000266.

Kollias, P., E. E. Clothiaux, B. A. Albrecht, M. A. Miller, K. P. Moran, and K. L. Johnson, 2005: The Atmospheric Radiation Measurement Program cloud profiles radars: An evaluation of signal processing and sampling strategies. *J. Atmos. Oceanic Technol.*, **22**, 930–948, https://doi.org/10.1175/JTECH1749.1.

Kuo, Y.-H., J. D. Neelin, and C. R. Mechoso, 2017: Tropical convective transition statistics and causality in the water vapor–precipitation relation. *J. Atmos. Sci.*, **74**, 915–931, https://doi.org/10.1175/JAS-D-16-0182.1.

Liebmann, B., G. N. Kiladis, and L. Carvalho, 2009: Origin of convectively coupled Kelvin waves over South America. *J. Climate*, **22**, 300–315, https://doi.org/10.1175/2008JCLI2340.1.

Machado, L. A. T., H. Laurent, N. Dessay, and I. Miranda, 2004: Seasonal and diurnal variability of convection over the Amazonia: A comparison of different vegetation types and large scale forcing. *Theor. Appl. Climatol.*, **78**, 61–77, https://doi.org/10.1007/s00704-004-0044-9.

——, and Coauthors, 2014: The CHUVA project. How does convection vary across Brazil? *Bull. Amer. Meteor. Soc.*, **95**, 1365–1380, https://doi.org/10.1175/BAMS-D-13-00084.1.

Marengo, J. A., and Coauthors, 2012: Recent developments in South American monsoon system. *Int. J. Climatol.*, **32**, 1–21, https://doi.org/10.1002/joc.2254.

Martin, S. T., and Coauthors, 2016: Introduction: Observations and modeling of the Green Ocean Amazon (GoAmazon2014/5). *Atmos. Chem. Phys.*, **16**, 4785–4797, https://doi.org/10.5194/acp-16-4785-2016.

——, and Coauthors, 2017: The Green Ocean Amazon experiment (GoAmazon2014/5) observes pollution affecting gases,

aerosols, clouds, and rainfall over the rain forest. *Bull. Amer. Meteor. Soc.*, **98**, 981–997, https://doi.org/10.1175/BAMS-D-15-00221.1.

Martinez, J. A., and F. Dominguez, 2014: Sources of atmospheric moisture for the La Plata River basin. *J. Climate*, **27**, 6737–6753, https://doi.org/10.1175/JCLI-D-14-00022.1.

McFarlane, S. A., C. N. Long, and J. Flaherty, 2013: A climatology of surface cloud radiative effects at the ARM tropical western Pacific sites. *J. Appl. Meteor. Climatol.*, **52**, 996–1013, https://doi.org/10.1175/JAMC-D-12-0189.1.

Muller, C. J., L. E. Back, P. A. O'Gorman, and K. A. Emanuel, 2009: A model for the relationship between tropical precipitation and column water vapor. *Geophys. Res. Lett.*, **36**, L16804, https://doi.org/10.1029/2009GL039667.

Neelin, J. D., K. Hales, and O. Peters, 2009: The transition to strong convection. *J. Atmos. Sci.*, **66**, 2367–2384, https://doi.org/10.1175/2009JAS2962.1.

Rehbein, A., T. Ambrizzi, and C. R. Mechoso, 2017: Mesoscale convective systems over the Amazon basin. Part I: Climatological aspects. *Int. J. Climatol.*, **38**, 215–229, https://doi.org/10.1002/joc.5171.

——, ——, ——, S. A. I. Espinosa, and T. A. Myers, 2019: Mesoscale convective systems over the Amazon basin: The GoAmazon2014/5 program. *Int. J. Climatol.*, **39**, 5599–5618, https://doi.org/10.1002/joc.6173.

Roundy, P. E., 2008: Analysis of convectively coupled Kelvin waves in the Indian Ocean MJO. *J. Atmos. Sci.*, **65**, 1342–1359, https://doi.org/10.1175/2007JAS2345.1.

Rowe, A. K., and R. A. Houze Jr., 2014: Microphysical characteristics of MJO convection over the Indian Ocean during DYNAMO. *J. Geophys. Res. Atmos.*, **119**, 2543–2554, https://doi.org/10.1002/2013JD020799.

——, ——, S. Brodzik, and M. D. Zuluaga, 2019: The diurnal and microphysical characteristics of MJO rain events during DYNAMO. *J. Atmos. Sci.*, **76**, 1975–1988, https://doi.org/10.1175/JAS-D-18-0316.1.

Schiro, K. A., J. D. Neelin, D. K. Adams, and B. R. Lintner, 2016: Deep convection and column water vapor over tropical land versus tropical ocean: A comparison between the Amazon and the tropical western Pacific. *J. Atmos. Sci.*, **73**, 4043–4063, https://doi.org/10.1175/JAS-D-16-0119.1.

——, F. Ahmed, S. E. Giangrande, and J. D. Neelin, 2018: GoAmazon2014/5 campaign points to deep-inflow approach to deep convection across scales. *Proc. Natl. Acad. Sci. USA*, **115**, 4577–4582, https://doi.org/10.1073/pnas.1719842115.

Schumacher, C., and A. Funk, 2018: GoAmazon2014/5 rain rates from the SIPAM Manaus S-band radar. ARM, accessed 6 August 2019, https://doi.org/10.5439/1459578.

——, R. A. Houze Jr., and I. Kraucunas, 2004: The tropical dynamical response to latent heating estimates derived from the TRMM Precipitation Radar. *J. Atmos. Sci.*, **61**, 1341–1358, https://doi.org/10.1175/1520-0469(2004)061<1341:TTDRTL>2.0.CO;2.

Straub, K. H., and G. N. Kiladis, 2002: Observations of a convectively-coupled Kelvin wave in the eastern Pacific ITCZ. *J. Atmos. Sci.*, **59**, 30–53, https://doi.org/10.1175/1520-0469(2002)059<0030:OOACCK>2.0.CO;2.

Takayabu, Y. N., 1994: Large-scale cloud disturbances associated with equatorial waves. *J. Meteor. Soc. Japan*, **72**, 433–449, https://doi.org/10.2151/jmsj1965.72.3_433.

——, and M. Murakami, 1991: The structure of super cloud clusters observed in 1-20 June 1986 and their relationship to easterly waves. *J. Meteor. Soc. Japan*, **69**, 104–125, https://doi.org/10.2151/jmsj1965.69.1_105.

Tang, S., and Coauthors, 2016: Large-scale vertical velocity, diabatic heating and drying profiles associated with seasonal and diurnal variations of convective systems observed in the GoAmazon2014/5 experiment. *Atmos. Chem. Phys.*, **16**, 14 249–14 264, https://doi.org/10.5194/acp-16-14249-2016.

Tulich, S. N., and G. N. Kiladis, 2012: Squall lines and convectively coupled gravity waves in the tropics: Why do most cloud systems propagate westward? *J. Atmos. Sci.*, **69**, 2995–3012, https://doi.org/10.1175/JAS-D-11-0297.1.

Vera, C., and Coauthors, 2006: Toward a unified view of the American monsoon systems. *J. Climate*, **19**, 4977–5000, https://doi.org/10.1175/JCLI3896.1.

Welty, J., S. Stillman, X. Zeng, and J. Santanello, 2020: Increased likelihood of appreciable afternoon rainfall over wetter or drier soils dependent upon atmospheric dynamic influence. *Geophys. Res. Lett.*, **47**, e2020GL087779, https://doi.org/10.1029/2020GL087779.

Wheeler, M., and G. N. Kiladis, 1999: Convectively coupled equatorial waves: Analysis of clouds and temperature in the wavenumber–frequency domain. *J. Atmos. Sci.*, **56**, 374–399, https://doi.org/10.1175/1520-0469(1999)056<0374:CCEWAO>2.0.CO;2.

——, ——, and P. J. Webster, 2000: Large-scale dynamical fields associated with convectively coupled equatorial waves. *J. Atmos. Sci.*, **57**, 613–640, https://doi.org/10.1175/1520-0469(2000)057<0613:LSDFAW>2.0.CO;2.

Yasunaga, K., and B. Mapes, 2012: Differences between more divergent and more rotational types of convectively coupled equatorial waves. Part I: Space–time spectral analyses. *J. Atmos. Sci.*, **69**, 3–16, https://doi.org/10.1175/JAS-D-11-033.1.

Zhuang, Y., R. Fu, J. A. Marengo, and H. Wang, 2017: Seasonal variation of shallow-to-deep convection transition and its link to the environmental conditions over the central Amazon. *J. Geophys. Res. Atmos.*, **122**, 2649–2666, https://doi.org/10.1002/2016JD025993.